

LUDWIG-MAXIMILIANS-UNIVERSITÄT MÜNCHEN

FAKULTÄT DER PHYSIK

Berechnung von renormierten Parametern für das
Anderson Impurity Model

Bachelorarbeit
im Studiengang 'Physik BSc'

vorgelegt von
Nick Nan Zhou

Betreuer: Professor Jan von Delft

Ablieferungstermin: 31.7.2019

Matrikelnr.: 11593120

LUDWIG-MAXIMILIANS-UNIVERSITÄT MÜNCHEN

FACULTY OF PHYSICS

Calculation of Renormalized Parameters for the Anderson Impurity Model

Nick Nan Zhou

Bachelor's Thesis

Physik BSc

submitted by

Nick Nan Zhou

Supervisor: Professor Jan von Delft

Date of submission: July 31, 2019

Immatriculation number: 11593120

Contents

1	Introduction	3
2	Single-Orbital Case	4
2.1	Calculating Renormalized Parameters	5
2.1.1	Effective Hybridization and Effective Impurity Energy Level	6
2.1.2	Calculation of Parameters via the Self-Energy	7
2.1.3	Comparing the Calculation Methods	8
2.1.4	Effective Interaction Energy	9
2.2	Convergence of Renormalized Parameters	9
2.3	Effective Parameters in Dependence of the Filling and Coulomb Interaction strength	10
3	Two-Orbital Anderson Model with Hund's Coupling	14
3.1	Calculations of the Effective Interaction for Small J at Half-Filling	15
3.2	Splitting of the Effective Interaction	16
3.3	Calculations of the Parameters for Large U and J at Half-Filling	21
3.4	Effective Interaction with Broken Particle-Hole Symmetry	23
4	Conclusion	24

Abstract

We show how to calculate renormalized parameters in order to describe the single-orbital Anderson impurity model and the two-orbital Anderson Impurity model with Hund's coupling as a Fermi liquid. In the two-orbital case we also show that the effective interaction depends on the kind of excitation and that it can be separated into two different parts. Furthermore, we analyze and interpret the behaviour of these renormalized parameters upon varying the bare parameters of the system.

1 Introduction

The Single Anderson impurity model describes a single impurity in a bath of electrons, where the impurity electrons interact with each other via the Coulomb interaction. The Hamiltonian can generally be written in the following form:

$$\begin{aligned}
 H_{\text{SIAM}} &= H_{\text{imp}} + H_{\text{int}} + H_{\text{bath}} + H_{\text{hyb}} = \\
 &= \sum_{\sigma,m} \epsilon_{d,m} d_{\sigma,m}^\dagger d_{\sigma,m} + H_{\text{int}} + \sum_{k,\sigma} \epsilon_{k,\sigma} c_{k,\sigma}^\dagger c_{k,\sigma} + \sum_{k,\sigma,m} \left(V_k d_{\sigma,m}^\dagger c_{k,\sigma} + V_k^* c_{k,\sigma}^\dagger d_{\sigma,m} \right). \quad (1)
 \end{aligned}$$

The term H_{imp} denotes the Hamiltonian for the energy due to the occupancy of the impurity orbitals. The interaction Hamiltonian is denoted by H_{int} and thus will depend on which interactions between the impurity electrons we consider. The direct energy contribution due to the bath is given by H_{bath} and the hopping of electrons between the bath and the impurity, that is to say the hybridization, is described by H_{hyb} . The creation operator for an electron at the impurity site in the orbital m with spin σ is denoted by $d_{\sigma,m}^\dagger$ and $\epsilon_{d,m}$ is the energy level for the impurity electrons in the orbital m . The operator $n_{d,\sigma,m} = d_{\sigma,m}^\dagger d_{\sigma,m}$ then denotes the number operator for impurity electrons with spin σ in orbital m . The energy of a single bath electron $\epsilon_{k,\sigma}$ is given by the dispersion relation of the bath electrons. The creation operator of a bath electron with wave vector k and spin σ is $c_{k,\sigma}^\dagger$ and the hybridization occurs via the matrix element V_k .

In the case of low-energy excitations the spectrum and self-energy of the Anderson impurity Model can be calculated via the numerical renormalization group (NRG). The procedure involves approximating the Hamiltonian as an impurity that couples to a semi-infinite chain instead of the bath-electrons.

The NRG program used in this thesis was provided by F.Kugler and is based on routines written by S.-S.Lee and A.Weichselbaum. However, the necessary code to conduct the following calculations and evaluate their results still had to be written by me.

The single Anderson impurity model is of interest due to its flexibility in applications. For example, it is closely related to the Kondo model, which describes a magnetic impurity interacting with a non-magnetic bath. The single Anderson impurity model can also describe a quantum dot, a quantum particle spatially restricted to such an extent that quantum mechanical effects can occur. Another motivation is its use in dynamical mean-field theory (DMFT) where lattice models of strongly correlated electrons can be mapped onto the Anderson impurity model [2].

Hewson et al. found a way to calculate attributes, such as the susceptibilities or the conductivity contribution due to the impurity, by describing the model as a Fermi liquid with renormalized parameters [3].

Fermi liquids are used to describe a system of interacting fermions at low temperatures and explain their similarities to the ideal Fermi gas, a non-interacting collection of fermions. The differences between the ideal Fermi gas and Fermi liquids generally manifest in the properties of the fermions taking on a new effective value, e.g. electrons that have a significantly larger effective mass than their physical mass.

The renormalized single impurity Anderson model depends on the three parameters: the effective level energy $\tilde{\epsilon}_d$, the effective hybridization strength \tilde{V} , and the quasiparticle interaction \tilde{U} .

The subject matter covered in this thesis is the following:

In section 2 we outline how to generally calculate the renormalized parameters. We then show the results of the calculations for the single-orbital case, where we vary the bare parameters ϵ_d and U . In section 3 we transition to the two-orbital case with Hund's coupling and also present

the results of the calculations upon varying the bare parameters, including the additional parameter we obtain through Hund's coupling. The effective interaction is then proven to be separable into two different kinds of contributions. The section concludes with the analysis of the behaviour of the effective interaction upon varying of the filling.

2 Single-Orbital Case

In the case single-orbital case the Hamiltonian of the model is given by

$$H_{\text{SIAM}} = \sum_{\sigma} \epsilon_d d_{\sigma}^{\dagger} d_{\sigma} + U n_{d,\uparrow} n_{d,\downarrow} + \sum_{k,\sigma} \epsilon_{k,\sigma} c_{k,\sigma}^{\dagger} c_{k,\sigma} + \sum_{k,\sigma} (V_k d_{\sigma}^{\dagger} c_{k,\sigma} + V_k^* c_{k,\sigma}^{\dagger} d_{\sigma}), \quad (2)$$

where the omission of the index m implies that we only have a single orbital. The interaction term $H_{\text{int}} = U n_{d,\uparrow} n_{d,\downarrow}$ describes the Coulomb interaction between the impurity electrons, thus $U > 0$ since electrons are repulsive to each other. The entire influence of the bath on the impurity is determined by the spectral function of the hybridization $\Delta(\omega)$ given by [1]

$$\mathcal{A}_{\Delta}(\omega) = \pi \sum_k |V_k|^2 \delta(\omega - \epsilon_k). \quad (3)$$

As one can see the spectral function of the hybridization is intimately linked with the hopping elements between the bath and impurity. In this thesis we use a rectangular symmetric function with length $2D$ and amplitude $0.1D$ as $\mathcal{A}_{\Delta}(\omega)$. The mathematical representation is therefore:

$$\mathcal{A}_{\Delta}(\omega) = 0.1D \cdot \Theta(D - |\omega|). \quad (4)$$

We use D as the energy unit so we can set $D = 1$.

As mentioned before, this function is discretized in order to approximate the Hamiltonian. Logarithmic discretization intervals are chosen, as doing so provides a good resolution on the low energy scale, while not making the computation impossibly difficult [1]. How fine the intervals are is given by the discretization parameter Λ . After the discretization the hopping elements t_n are calculated, which connect the bath sites to a chain. Since the discretization intervals cannot be infinitely many we do not end up with a semi-infinite chain, but a chain of N bath sites instead. The only site left is the impurity site, which has to couple to the chain with a parameter V , that can also be calculated from the hybridization function (4). Thus the Hamiltonian takes on the form

$$H_{\text{SIAM}}^N = \sum_{\sigma} \epsilon_d d_{\sigma}^{\dagger} d_{\sigma} + U n_{d,\uparrow} n_{d,\downarrow} + V \sum_{\sigma} \left(d_{\sigma}^{\dagger} c_{1,\sigma} + c_{1,\sigma}^{\dagger} d_{\sigma} \right) + \sum_{n=1,\sigma}^{n=N-1} t_n \left(c_{n,\sigma}^{\dagger} c_{n+1,\sigma} + c_{n+1,\sigma}^{\dagger} c_{n,\sigma} \right), \quad (5)$$

where $c_{n,\sigma}^{(\dagger)}$ are the operators of the conduction electron of the n -th site of the chain. In our convention the first bath site has the index 1, and we have N bath sites as a whole.

The actual calculation is then done by starting out with one bath site, diagonalizing and then iteratively adding additional sites and diagonalizing again. Since the number of states grows exponentially with each diagonalization step, at some point the higher energy states have to be omitted, which causes the kept higher-energy states to be less accurate than the low energy excitations that we are more interested in. For further information on NRG refer to [1].

2.1 Calculating Renormalized Parameters

In order to calculate the renormalized parameters we need certain excitation energies, that can be taken from the low energy excitation spectrum calculated via NRG. Since the spectrum is calculated by iteratively adding sites we get a different spectrum each time another site is added. We can thus plot the different excitation energies against the length of the chain N , which results in a so-called flow diagram. If the calculations are accurate enough the excitation energies converge for sufficiently large N [1]. It should be noted that the excitation energies calculated via NRG are not the actual physical excitation energies, as a factor $\Lambda^{(N-1)/2}$ is multiplied in order to get the energies to converge for large N . So even after correctly selecting the excitation energies we still have to multiply a factor $\Lambda^{-(N-1)/2}$ in order to obtain the actual excitation energies.

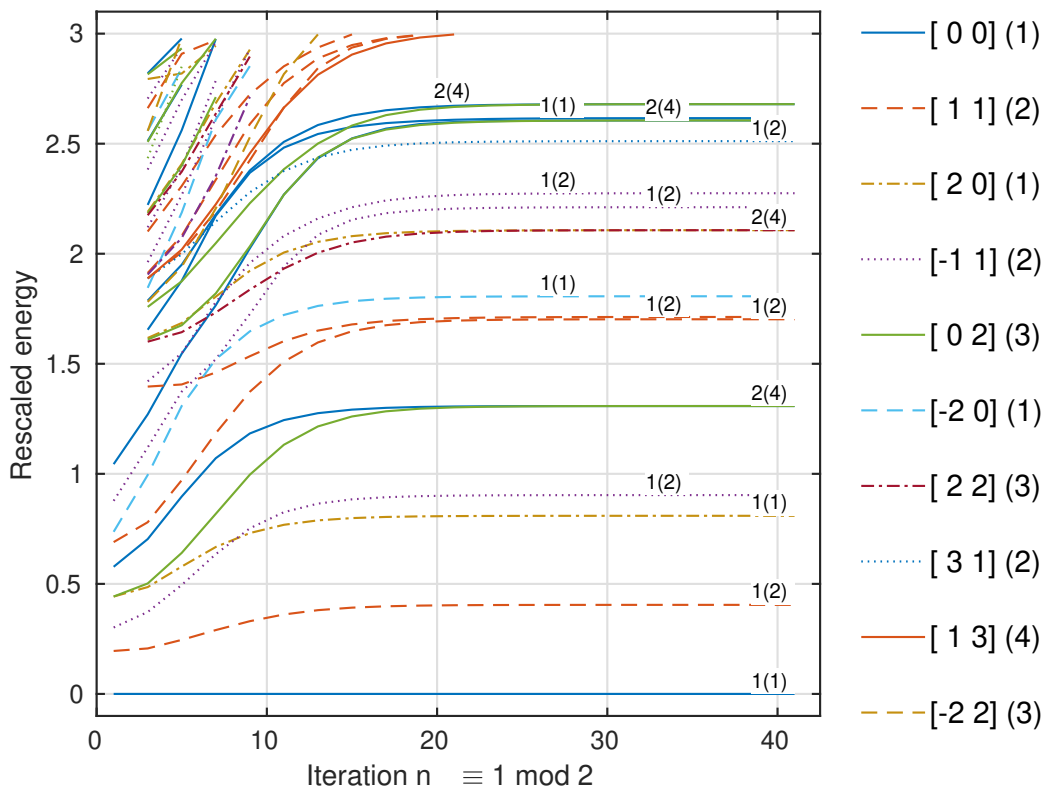


Figure 1: Flow diagram for the single channel case with $U = 0.3 = -\epsilon_d$. The energies converge for sufficiently large N . The excitations are differentiated via the quantum numbers U(1)-charge and SU(1)-spin.

In figure 1 we can see an example flow diagram, which is calculated at $U = \epsilon_d = -0.3$, where ϵ_d is chosen such that we do not find ourselves at half-filling, since then the particle- and hole-excitation energies cannot be differentiated. As one can see, the lines are separated by their corresponding quantum numbers. One can choose different quantum numbers to separate the lines. In our case the U(1)-charge, which is the first number, and the SU(2)-spin, which is the second number, are chosen. The third number in brackets is the degeneracy, thus 1 corresponds to a singlet state and 3 corresponds to a triplet state.

The flow diagrams for even and uneven N have to be separated as their energy spectra differ to a large degree. In this work we only look at uneven N , as the calculation for even N is

considerably more difficult, mainly due to the fact that the ground state is degenerate. The excitations we are going to be interested in are:

- single-particle excitations
- single-hole excitations
- two-particle excitations
- two-hole excitations
- particle-hole excitations

The lowest particle excitation energy in this example is the dashed line with the corresponding numbers [1 1] (2), since particles contribute a charge of 1. For single particle and hole excitations the two-fold degenerate state, indicated by the second 1 or the 2 in brackets, is the only possible spin state.

For hole excitations the procedure is analogous, resulting in the dotted purple line with numbers [-1 1] (2) being selected.

When it comes to selecting the two-particle or two-hole excitations the first number has to be a 2 or -2. In the case of particle-hole excitations the two charges should add up to 0, which means that one has to avoid picking the ground state energy as the lowest excitation energy, since that is not an excitation. Due to the fact that two fermion excitations can combine to either a spin singlet or triplet state the second number can be a 1 or 0. We will not consider the spin-triplet excitations in the single-channel case, as the excitation energies are too high.

2.1.1 Effective Hybridization and Effective Impurity Energy Level

Next we want to look at the Green's function of the impurity site if there is no interaction

$$G_{00}(\omega) = \frac{1}{\omega - \epsilon_d - V^2 g_{11}(\omega)}, \quad (6)$$

where $g_{ii}(\omega)$ describes the Green's function of the free chain where every site up to the i -th site is removed. For example, g_{11} would be the non-interacting chain without the impurity site. This Green's function can be calculated by a recursive relation [3]:

$$g_{ii}(\omega) = \frac{1}{\omega - t_i^2 g_{i+1, i+1}(\omega)} \quad \text{and} \quad g_{NN} = \frac{1}{\omega}. \quad (7)$$

The excitation energies are given by the poles of the Green's function:

$$\omega \stackrel{!}{=} \epsilon_d + V^2 g_{11}(\omega). \quad (8)$$

If the model can be described by a renormalized theory then the transition to the interacting model should be possible by simply replacing the bare parameters ϵ_d and V^2 with their renormalized counterparts $\tilde{\epsilon}_d$ and \tilde{V}^2 . The lowest single hole and particle excitation energies are then given by the poles of the Green's function, resulting in the relations

$$\begin{aligned} E_p(N) &= \tilde{\epsilon}_d(N) + \tilde{V}^2 g_{11}(E_p(N)), \\ -E_h(N) &= \tilde{\epsilon}_d(N) + \tilde{V}^2 g_{11}(-E_h(N)). \end{aligned} \quad (9)$$

From these relations, we can derive expressions for $\tilde{\Delta}$ and $\tilde{\epsilon}_d$:

$$\tilde{V}^2(N) = \frac{E_p(N) + E_h(N)}{g_{11}(E_p(N)) - g_{11}(-E_h(N))}. \quad (10)$$

$$\tilde{\epsilon}_d(N) = \frac{g_{11}(E_p(N))E_h(N) + g_{11}(-E_h(N))E_p(N)}{g_{11}(-E_h(N)) - g_{11}(E_p(N))}. \quad (11)$$

It should be noted that sometimes the rescaled energies from the NRG calculation are used, which introduce several $\Lambda^{(N-1)/2}$ factors. In this work we use the actual physical excitation energies.

The chain Hamiltonian comes closer to describing the actual model the longer the chain is. Therefore the values of $\tilde{V}^2(N)$ and $\tilde{\epsilon}_d(N)$ should converge for large N , if the actual model can be described by a renormalized model. We can then define these converged values as the renormalized parameters.

2.1.2 Calculation of Parameters via the Self-Energy

The NRG procedure allows one to not just calculate an approximation of the energy spectrum but also the self-energies for different frequencies, which lets us directly calculate some of the renormalized parameters through NRG.

The Green's function can be written in the form

$$G(\omega) = \frac{1}{\omega - \epsilon_d - \Delta(\omega) - \Sigma(\omega)}, \quad (12)$$

where $\Sigma(\omega)$ is the self-energy and $\Delta(\omega)$ is the hybridization. The hybridization describes the coupling between the non-interacting chain and the impurity, thus like before we can write $\Delta(\omega)$ as $V^2 g_{11}(\omega)$, where $g_{11}(\omega)$ is the Green's function of the non-interacting chain defined in the section before. If the model is viewed as a Fermi liquid the Green's function should have the form

$$G(\omega) = \frac{Z}{\omega - \tilde{\epsilon}_d - \tilde{\Delta}(\omega)} = \frac{Z}{\omega - \tilde{\epsilon}_d - \tilde{V}^2 g(\omega)}, \quad (13)$$

where Z is the quasiparticle weight. Since we find ourselves in a low energy regime we can approximate the self-energy with a first order Taylor expansion, so $\Sigma(\omega) \approx \Sigma(0) + \Sigma'(0)\omega$. If we insert this expression into (12) and reorder we get

$$\frac{1}{1 - \Sigma'(0)} \cdot \frac{1}{\omega - \frac{\epsilon_d + \Sigma(0)}{1 - \Sigma'(0)} - \frac{V^2 g_{11}(\omega)}{1 - \Sigma'(0)}}. \quad (14)$$

Comparing this with the Fermi-liquid Green's function (13), it becomes clear how to define the renormalized parameters in dependence of the bare parameters and the self-energy:

$$Z = \frac{1}{1 - \Sigma'(0)} \quad \tilde{\epsilon}_d = \frac{\epsilon_d + \Sigma(0)}{1 - \Sigma'(0)} = Z(\epsilon_d + \Sigma(0)) \quad \tilde{V}^2 = \frac{V^2}{1 - \Sigma'(0)} = Z \cdot V^2. \quad (15)$$

There is another renormalized parameter that is of interest; the effective quasiparticle interaction \tilde{U} . Its relation to the four-vertex $\Gamma(\omega_1, \omega_2, \omega_3, \omega_4)$ at zero frequency is given by [3]

$$\tilde{U} = Z^2 \Gamma(0, 0, 0, 0). \quad (16)$$

In this work, we from now on only refer to the four-vertex at zero frequency, thus the (0,0,0,0) is omitted.

2.1.3 Comparing the Calculation Methods

We have established that the renormalized parameters can either be directly calculated through NRG or by looking at the poles of the Green's function. In this section we look at the differences in the results of the two calculation methods.

The self-energy calculations via NRG can be made a lot more accurate through the usage of z -shifts. This procedure entails slightly changing the discretization intervals with an exponent $z \in [0, 1)$ and then averaging over the calculations of all the different z that were used. This obviously increases the computation time, since for each z the spectrum has to be recalculated. In this work the calculation of the self-energy was only used in certain cases to ensure that the results are consistent. Reason is that generally the calculation via the self-energy is only accurate and converges for a rather large number of z -shifts, making calculations much more time consuming. This is shown in the upper diagram in figure 2, where Z is calculated two different ways with $U = 0.3$ and $\epsilon_d = -U/2$, and plotted against the number of z -shifts. Z_Σ is calculated according to the first equation in (15) and Z_{RPT} is calculated by first calculating \tilde{V}^2 according to (10) and plugging it into the last equation in (15).

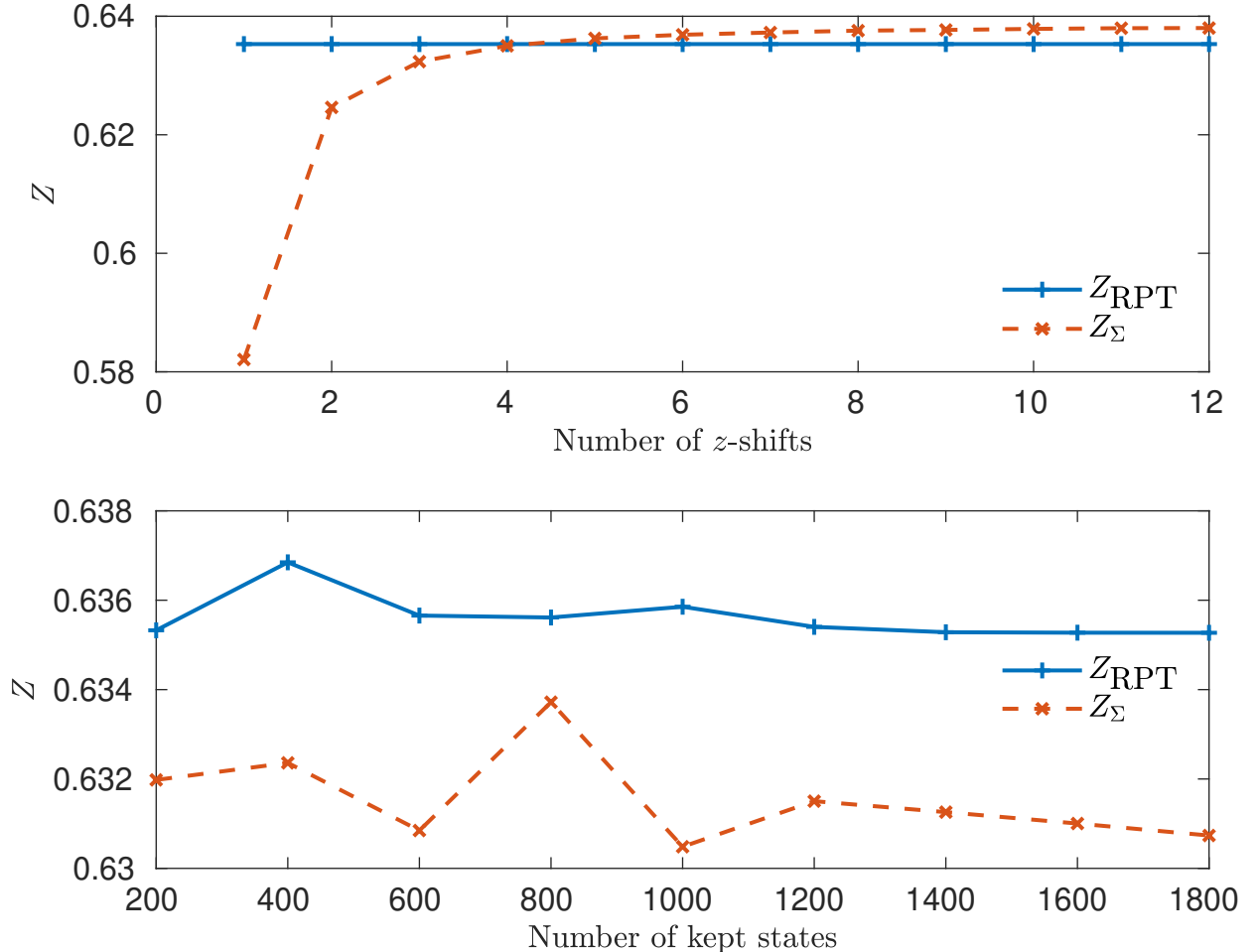


Figure 2: Comparing different Z calculated via the discrete spectrum and the self-energy for $\epsilon_d = -U/2 = -0.15$. In the upper plot we vary the number z -shifts while keeping the number of kept states at 2000. In the lower plot the number of states is varied and the number of z -shifts kept at 4. In both cases the calculation via the self-energy takes longer to converge.

One can also vary the number of states kept after each diagonalization step. Obviously a higher number of states is computationally more intensive, thus it is again of interest to choose a number as small as possible, while also keeping the results accurate. When plotting the Z calculated via the different methods against the number of kept states, as in the lower diagramm in figure 2, one can see that the Z calculated from the renormalized parameters fluctuate a lot less than the one calculated from the self-energy.

2.1.4 Effective Interaction Energy

The interaction term can only play a part in multiple hole or particle excitations. Therefore the effective interaction should be proportional to the difference between a two-particle (hole) excitation energy and twice the energy of a single excitation. The exact expression is given by [3]

$$E_{pp}(N) - 2E_p(N) = \tilde{U}(N)|\psi_{p,1}^*(0)|^2|\psi_{p,1}^*(0)|^2. \quad (17)$$

Where $|\psi_{p,1}(0)|^2$ is the absolute square of the wave function of the lowest single particle excitation at the first site i.e. the impurity site. It can be calculated by [3]

$$|\psi_{p,1}(0)|^2 = \frac{1}{1 - \tilde{V}^2(N)g'_{11}(E_p(N))}. \quad (18)$$

$g'_{ii}(\omega)$ denotes the derivatives of the Green's functions of non-interacting models from before. Thus

$$g'_{ii}(\omega) = \partial_\omega g_{ii}(\omega) = -\frac{1 - t_i^2 g'_{i+1,i+1}(\omega)}{(\omega - t_i^2 g_{i+1,i+1})^2} \quad \text{and} \quad g'_{NN}(\omega) = -\omega^{-2}. \quad (19)$$

One can also calculate the effective interaction based on two hole excitations and particle-hole excitations. For the hole-excitation calculation one has to substitute the E_{pp} , E_p and $|\psi_{p,1}(1)|^2$ with their hole counterpart. As for the particle-hole excitation, the sign also has to be switched, i.e. $E_p + E_h - E_{ph}$, since particles and holes attract each other and \tilde{U} should share the same sign.

An exact derivation of (17) is not given here, but just by looking at the formula one can intuitively understand why this expression would make sense: The energy difference between the a two particle excitation, as in the energy of the two single particles and their interaction energy, and two times the single particle excitation should simply be the interaction energy. This quasiparticle interaction energy is described by a prefactor \tilde{U} times the product of the two "charges", which are the wave functions at the impurity site. After calculating \tilde{U} and Z one can also calculate Γ according to (16).

2.2 Convergence of Renormalized Parameters

The system described by (5) is only an approximation of the Anderson impurity model, that we are actually interested in. How accurately (5) can describe this model depends on the number of sites N in the chain. Therefore only if the chain is long enough do we enter the regime where (5) can describe a system that can be seen as a Fermi liquid. Thus, if N is rather small, renormalized parameters that describe a Fermi liquid do not really exist. They only start to "become clear" as the length of the chain is increased, which is when the definitions (10), (11) and (17) converge to their respective values.

Earlier we defined the effective interaction \tilde{U} in three different ways according to (17): Via two-particle excitations as \tilde{U}_{pp} , two-hole excitations as \tilde{U}_{hh} and particle-hole excitations as \tilde{U}_{ph} . For short chains effective parameters that describe the interaction do not really exist, therefore it is not expected that the different \tilde{U} are the same in that case. When we reach

the Fermi liquid regime, however, one would expect \tilde{U} to only depend on the “charges” of the excitations, which can be expected to be the same for particles and holes, except for the sign, implying that the absolute values of the different \tilde{U} should also be the same. Additionally, since we defined \tilde{U}_{ph} with a flipped sign compared to \tilde{U}_{pp} and \tilde{U}_{hh} , the sign should be the same as well.

Indeed this is what we find if our NRG calculations were sufficiently accurate, as is shown in figure 3, where \tilde{U}_{pp} , \tilde{U}_{hh} and \tilde{U}_{ph} are plotted against the number of chain sites N for $U = -\epsilon_d = 0.3$, where ϵ_d was chosen such that we do not find ourselves at half filling, where the particle and hole excitation energies are identical, trivially making $\tilde{U}_{hh} = \tilde{U}_{pp}$. It should be noted that while in the current single-orbital case the values continuously converge for bigger N , in more complicated cases, like the two-orbital case that we will later look at, numerical instabilities arise for N that are too large, causing the calculated parameters to be inaccurate. In those cases we have to pick one of the N that is neither too large nor too small to be our convergence value.

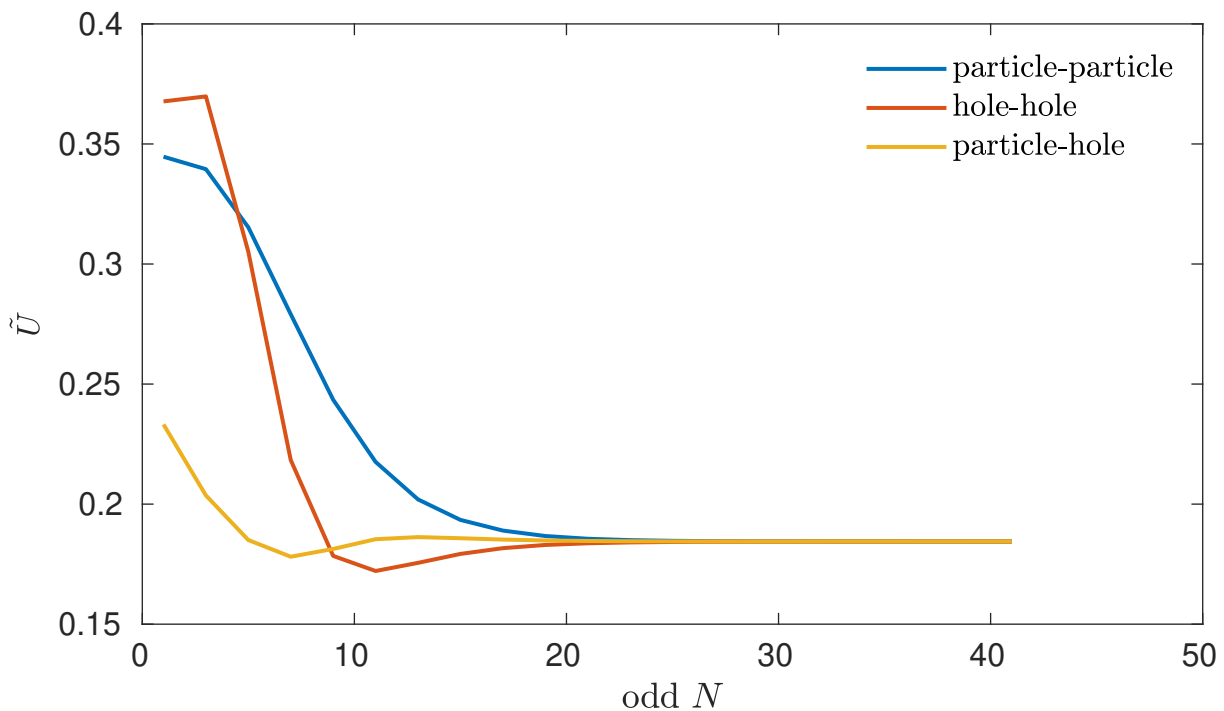


Figure 3: \tilde{U} calculated in three different ways from two particle, two hole and particle-hole excitations for $U = -\epsilon_d = 0.3$. We can see that only for large N do the different \tilde{U} converge to the same value.

2.3 Effective Parameters in Dependence of the Filling and Coulomb Interaction strength

After calculating $\tilde{\epsilon}_d$ (figure 4), \tilde{U} (figure 5), Γ (figure 6) and Z (figure 7) for different fillings, which are determined by the ratio ϵ_d/U , and Coulomb interaction strengths U , we can discuss the qualitative behaviour of the parameters:

From the colourplot in figure 4 we can see that the smallest absolute value of $\tilde{\epsilon}_d = 0$ is always found at half-filling and that $\tilde{\epsilon}_d$ seems to be point-symmetric around half-filling. From

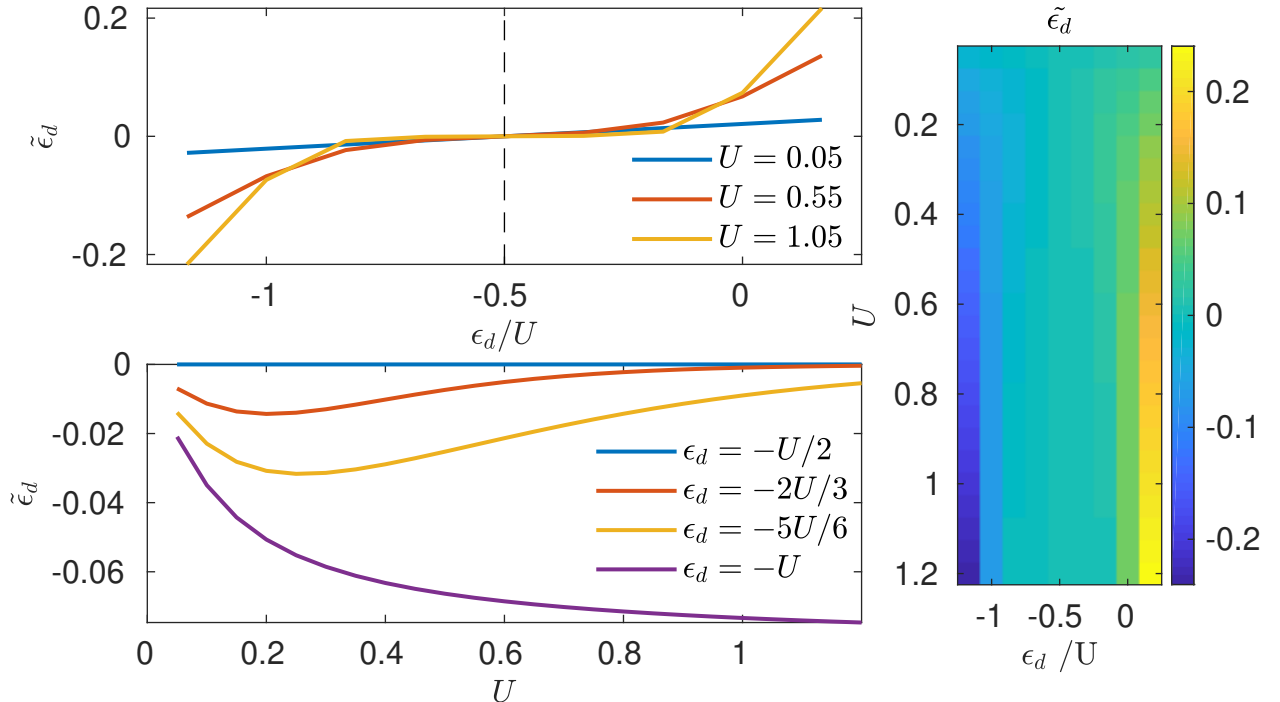


Figure 4: $\tilde{\epsilon}_d$ calculated for different U and ϵ_d/U . In the upper left lineplot we plot $\tilde{\epsilon}_d$ for three different U against ϵ_d/U , which determines the filling. The dashed black line indicates half-filling. Just below we fix the filling and vary U to get another lineplot.

the upper left lineplot we can see that when transitioning to the full-orbital regime, that is to say ϵ_d/U is increased, the effective energy level also increases. Analogously, when we transition to the empty-orbital regime, that is to say ϵ_d/U decreases, the effective level becomes negative and the absolute value increases just like when transitioning to the full-orbital regime. Therefore, $\tilde{\epsilon}_d$ is indeed point-symmetric around half filling. We can also see that an increase in U not only causes the increase of the absolute value of $\tilde{\epsilon}_d$ to become more drastic, but also more sudden. The result can be seen in the lower-left lineplot where we vary U instead of the filling. The effective local level energy $\tilde{\epsilon}_d$ has a minimum (or maximum if a $\tilde{\epsilon}_d > -U/2$ is chosen) that moves to higher U as the filling is decreased (increased).

Since the colour plots 5, 6 and 7 and the upper left line plots are symmetric, we can conclude that these parameters are symmetric around half-filling

If U is increased, \tilde{U} also increases initially, as one would naively expect, since an increase in the bare interaction should also increase the effective interaction. However, at some point \tilde{U} reaches a maximum and starts converging towards 0. This is shown in figure 5 in the lower left line plot. This behaviour can be explained by U suppressing charge fluctuations which implies screening causing a weakening of \tilde{U} . This screening effect apparently scales faster with an increasing U than the direct strength increase of the effective interaction. Therefore, at some point the screening effect starts to dominate causing the maximum, after which \tilde{U} continually decreases.

When we vary the filling and fix U , the minimum of the effective interaction is found at half-filling as can be seen in the upper left plot. Additionally, one can see that the further one strays away from half filling the larger \tilde{U} generally becomes and the maximum of \tilde{U} in dependence of U shifts to higher U , which is shown in the lower left plot. This implies that the screening is strongest around half-filling and that moving away makes it harder for the screening effect to

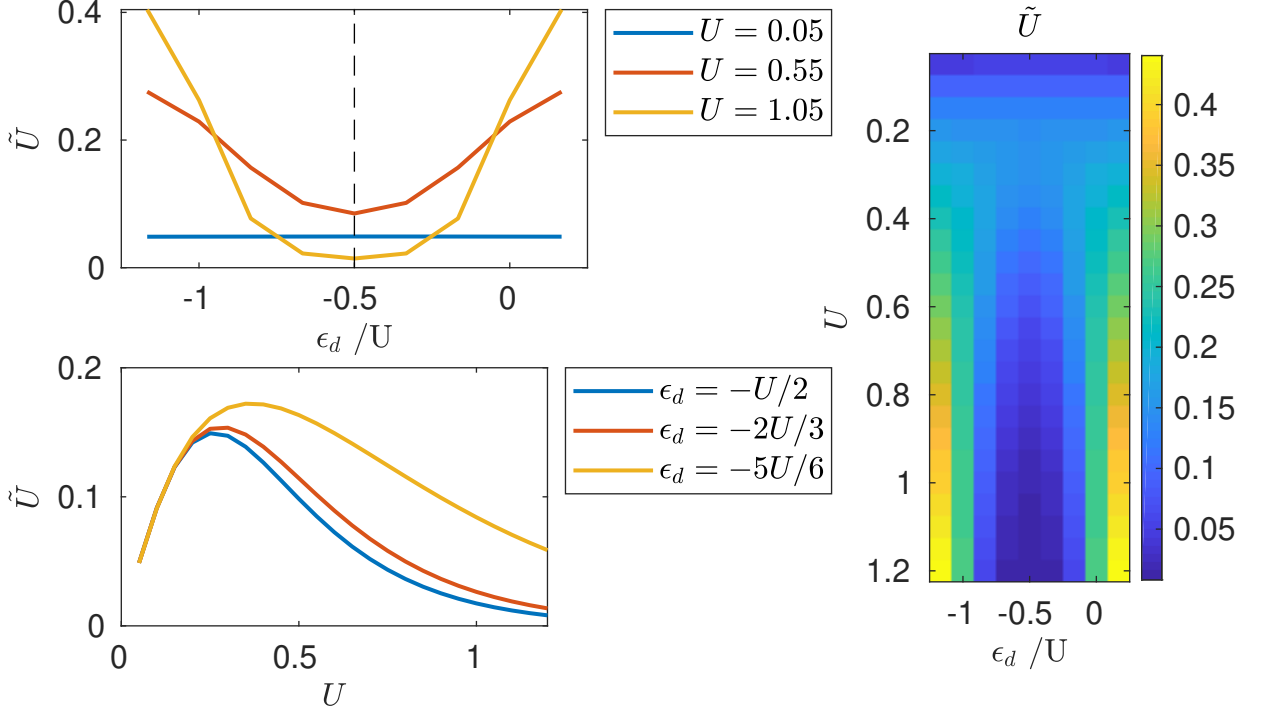


Figure 5: Similar structure to figure 4, but now \tilde{U} is calculated instead of $\tilde{\epsilon}_d$. In the upper left plot the filling is varied while fixing U and in the lower left plot U is varied at a fixed filling.

dominate the effective interaction \tilde{U} .

In the colour plot of figure 6 it is obvious the largest value of Γ is found at half filling with the largest U value. This is due to the monotonous behaviour of Γ , where decreasing U or moving away from half filling causes Γ to converge towards 0, as is evident by the lower and upper left line plot. This was also expected as Γ is the Coulomb interaction U between the actual physical particles plus all the higher-order Coulomb interactions that can occur. An increase in U is expected to increase all orders of interactions, thus Γ starts to diverge. The behaviour of Γ is also consistent with the results in \tilde{U} , as in that a stronger effective physical interaction causes the charge fluctuation suppression and thus the screening to also become more pronounced.

While Z also exhibits a monotonous behaviour, the pattern is the exact opposite to Γ , where for the largest Γ values, i.e. half-filling and large U , Z takes on its smallest values, which converge towards 0. Moving away from that point causes Z to take on its largest values, which converge towards 1. That is to be expected since Z can be seen as a measure of how strong the effects due to the interactions between the electrons are in comparison to a free system. If $Z = 1$ then the Green's functions of Fermi liquids are the same as for the non-interacting system which matches the behaviour of our effective physical interaction strength Γ converging towards 0. When Z goes towards 0 the differences to the free gas increase, that is to say the interactions become stronger, which again matches the behaviour of Γ .

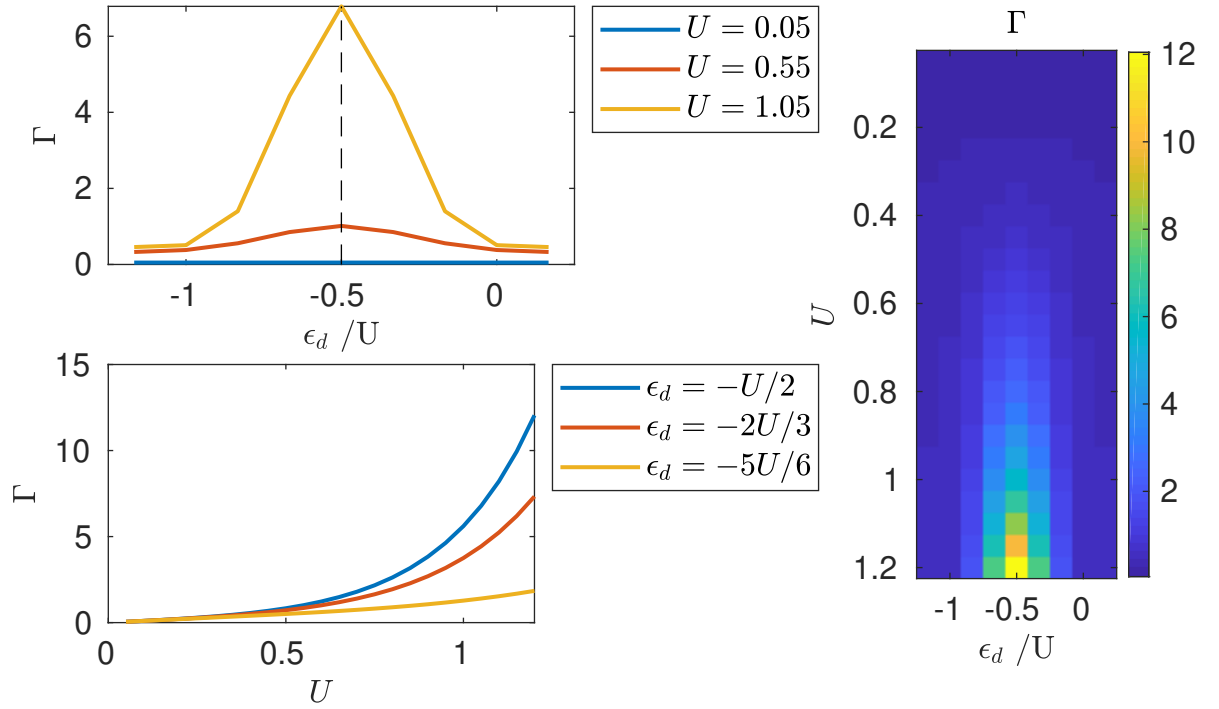


Figure 6: Analogous to figure 4 and 5, but here it shows the value of Γ . In the lineplots either U or the filling is varied and the other variable fixed. Unlike \tilde{U} the four-vertex Γ is completely monotonous.

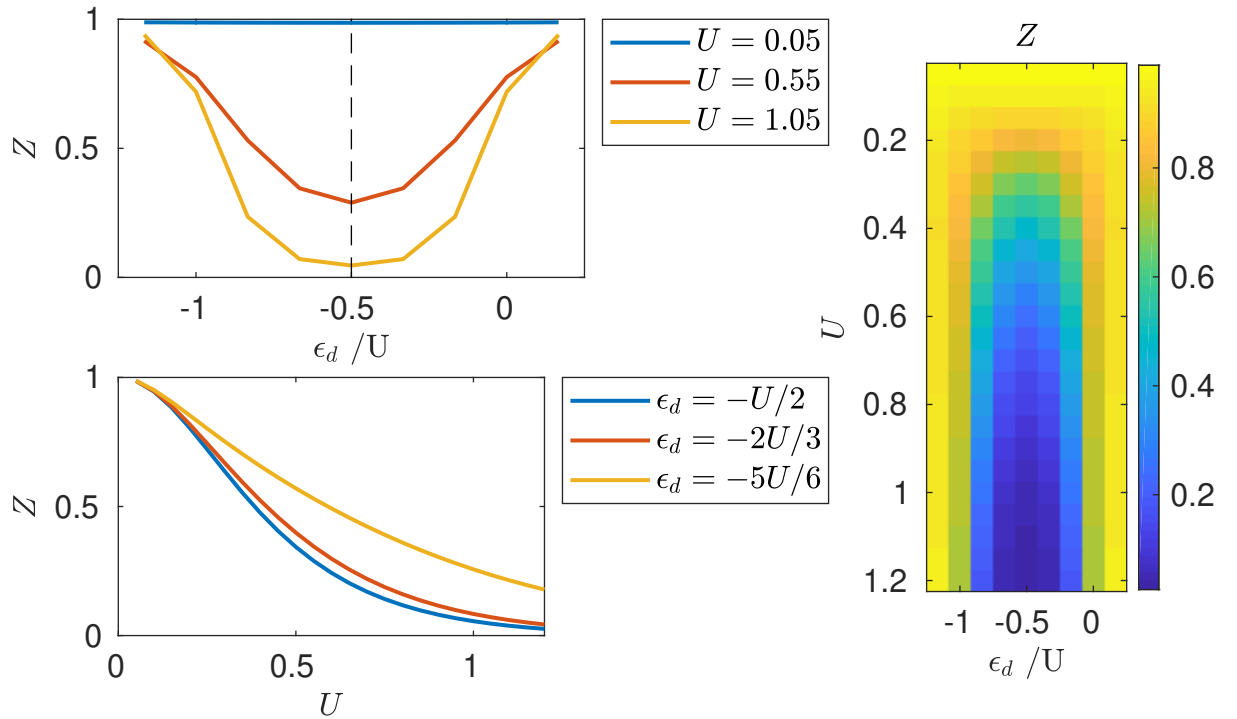


Figure 7: Analogous to the other figures in this subsection. This time the quasiparticle weight Z is calculated. The lineplots can either show a variation of the filling or U . Exhibits the opposite behaviour to Γ

3 Two-Orbital Anderson Model with Hund's Coupling

The Hamiltonian of the two-orbital case is similar to the single channel case. One big difference is that the creation and annihilation operators now have the additional index m which corresponds to which orbital the electron is in or is created in. We have two different orbitals in the two channel case:

$$H_{\text{SIAM}} = \sum_{m\sigma} \epsilon_d d_{m\sigma}^\dagger d_{m\sigma} + \sum_{k\sigma} \epsilon_{k\sigma} c_{k\sigma}^\dagger c_{k\sigma} + \sum_{km\sigma} \left(V_k d_{m\sigma}^\dagger c_{k\sigma} + V_k^* c_{k\sigma}^\dagger d_{m\sigma} \right) + H_{\text{int}}. \quad (20)$$

Another change is the new interaction term H_{int} , which can be written in the form:

$$\begin{aligned} H_{\text{int}} &= \frac{U}{2} \sum_{mm'\sigma\sigma'} d_{m\sigma}^\dagger d_{m'\sigma'}^\dagger d_{m'\sigma'} d_{m\sigma} + \frac{J}{2} \sum_{mm'\sigma\sigma'} d_{m\sigma}^\dagger d_{m'\sigma'}^\dagger d_{m\sigma'} d_{m'\sigma} \\ &= (U + J) \sum_m n_{d,m\uparrow} n_{d,m\downarrow} + U \sum_{m \neq m'} n_{d,m\uparrow} n_{d,m'\downarrow} \\ &\quad + (U - J) \sum_{m < m', \sigma} n_{d,m\sigma} n_{d,m'\sigma} - J \sum_{m \neq m'} d_{m\uparrow}^\dagger d_{m\downarrow} d_{m'\downarrow}^\dagger d_{m'\uparrow}. \end{aligned} \quad (21)$$

Where J is the new Hund's coupling interaction. The renormalized parameters are defined the same way as before.

The kinds of excitation energies we are going to be interested are the same one as before. However, the now possible different orbital configurations introduce another quantum number; the SU(2) orbital number. In figure 8 an example flow diagramm calculated at $U = 0.25$,

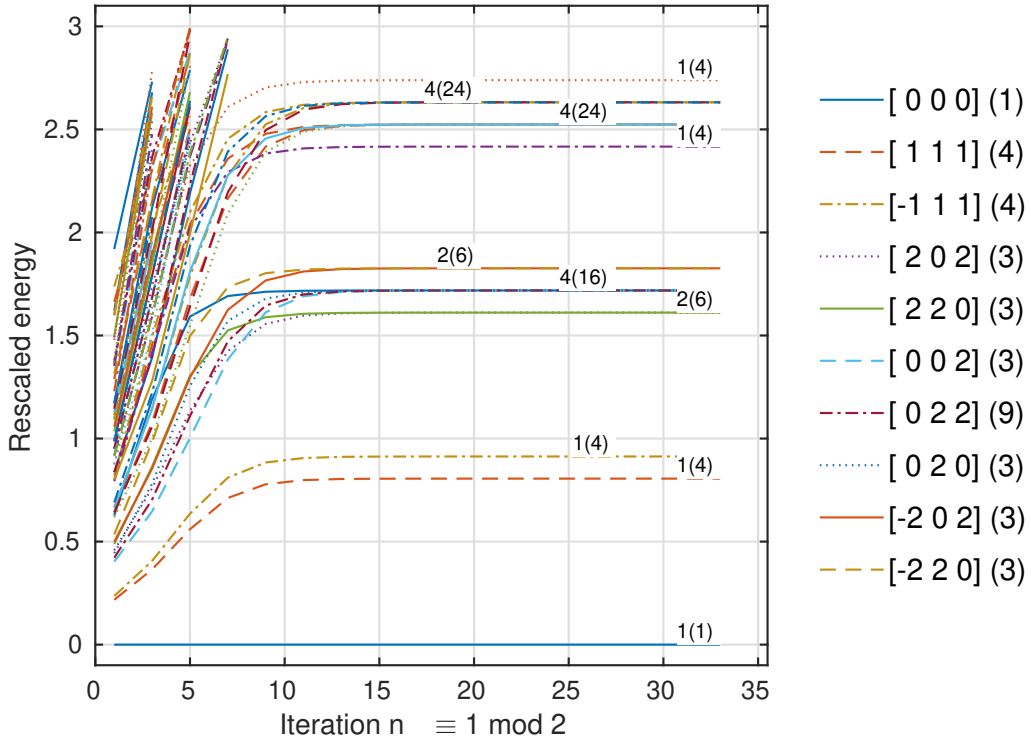


Figure 8: Flow diagramm for the 2-channel case with $U = 0.25$, $J = 0.04$ and $\epsilon_d = -3.3 \cdot U/2$. We now need an extra quantum number two differentiate the lines.

$J = 0.04$ and $\epsilon_d = -3.3 \cdot U/2$ is shown. The ϵ_d was again chosen such that we do not find

ourselves at half-filling, where we cannot differentiate the particle and hole excitation energies. The biggest difference in comparison to the single-channel case is that the lines are categorized by an additional quantum number. In this diagramm the first number is still the U(1) charge, but the second number is now the SU(2) orbital number and the third number the SU(2) spin. The selection of the single-particle or hole excitations is again straightforward, since there is only one possible quantum number configuration; $[1\ 1\ 1]$ (4) for one particle and $[-1\ 1\ 1]$ (4) for one hole. The four-fold degeneracy is due to the two-fold degeneracy of the spin and the two-fold degeneracy of the orbital number combining together.

The double excitations are again more complicated, since we need to differentiate between the different possible spin and orbital configurations. When selecting the spin singlet orbital singlet particle-hole excitation one again has to pay attention not to pick the ground state, because it shares the same quantum numbers. It is possible to have four different excitation energies for each kind of double excitation. However, the spin-singlet orbital-singlet and the spin-triplet orbital-triplet excitation energies are relatively high for two-particle and two-hole excitations, making the values too inaccurate.

3.1 Calculations of the Effective Interaction for Small J at Half-Filling

Unlike in the single-channel case, the effective interaction \tilde{U} and the four-vertex Γ depend on whether we look at two particle or particle-hole excitations, and what the other quantum numbers are, i.e. the SU(2)-spin S and the SU(2)-orbital number T . Therefore we define several $\tilde{U}_q^{S,T}$, where $q \in \{pp, hh, ph\}$ indicating whether $\tilde{U}_q^{S,T}$ was calculated from two-particle, two-hole or particle-hole excitations. We for now only look at the parameters at half-filling, which in the two channel case corresponds to $\epsilon_d = -3U/2$, starting with the spin-singlet orbital-triplet particle-particle excitation.

In the colour plot of figure 9, we can see that $\tilde{U}_{pp}^{S=0,T=1}$ is always positive. The lineplot also shows that there is a maximum when U is fixed and J is varied. After the maximum, $\tilde{U}_{pp}^{S=0,T=1}$ converges to 0 similar to the single channel case. The position of the maximum shifts towards smaller J values when U is increased. The increase in U also causes the value of the maximum to decrease. This is because additional orbital fluctuations exist that are not present in the single-channel case [4]. These orbital fluctuations can be suppressed by increasing J . Therefore both U and J have fluctuation-suppressing effects and thus cause screening. The result is the shifting maximum and the convergence towards 0 for large U and J .

Differences to the single-channel case become even more sharp when looking at the spin-triplet orbital-singlet particle-particle excitation. In the colourplot of figure 10 we can see that for sufficiently large U and J the sign of $\tilde{U}_{pp}^{S=1,T=0}$ becomes negative, which would correspond to an attraction of the quasiparticles despite them possessing the same charge! By again looking at the J - $\tilde{U}_{pp}^{S=1,T=0}$ plot shown on the left side of the figure we see that unlike before $\tilde{U}_{pp}^{S=1,T=0}$ starts to drop off immediately until it reaches a minimum with a negative value. At this point the screening effect due to the increasing J starts to dominate again causing $\tilde{U}_{pp}^{S=1,T=0}$ to converge to 0. However this time it converges from the negative side meaning that for all large U and J that the effective interaction is attractive. Similar to the spin-singlet and orbital-triplet case, an increasing U causes the absolute value of the minimum to decrease and the position to move towards smaller J values. Since $\tilde{U}_{pp}^{S=1,T=0}$ is positive for $J = 0$ and the minimum is negative, there exists a point at which $\tilde{U}_{pp}^{S=1,T=0}$ becomes 0 resulting in an effectively non-interacting system!

In the lineplots of figure 9 and 10 we also compare two particle excitations and particle-hole

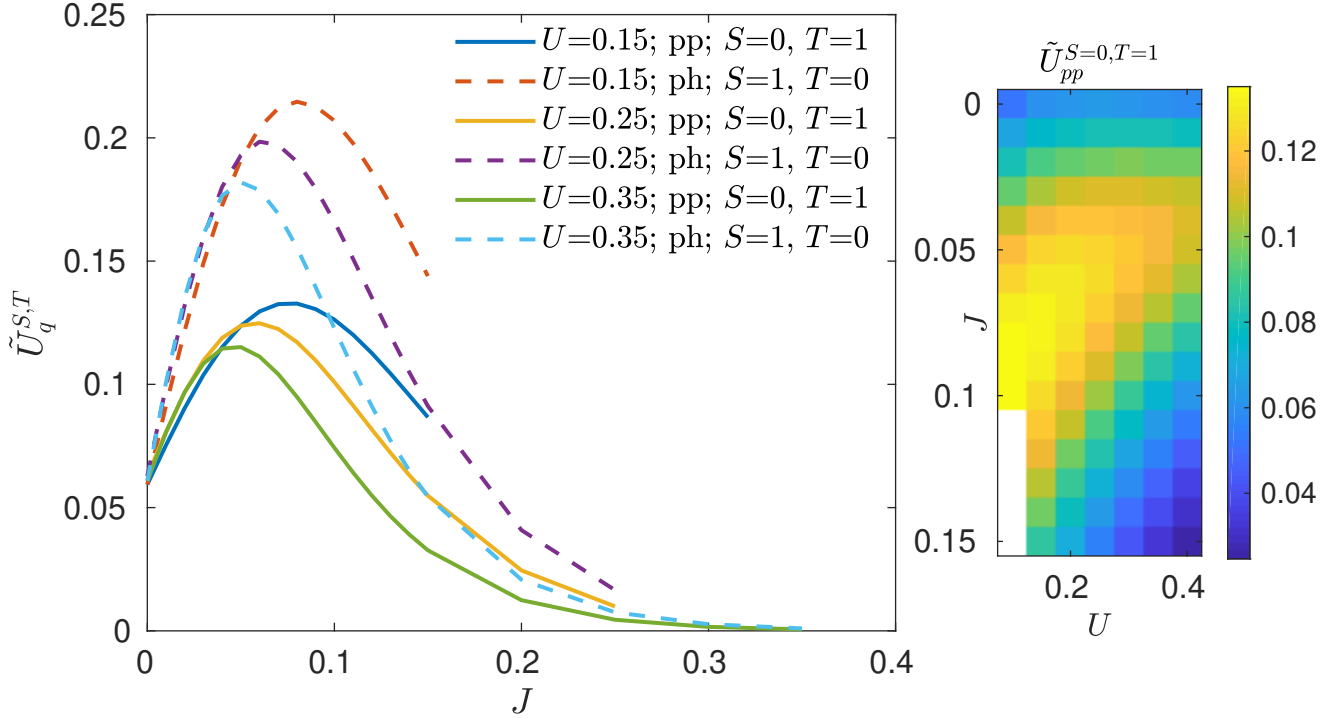


Figure 9: The effective interaction $\tilde{U}_{pp}^{S=0,T=1}$ calculated while the Coulomb strength U and Hund's coupling J is varied at half-filling, i.e. $\epsilon_d = -3U/2$. In the line plot U is fixed at different values and J is varied. $\tilde{U}_{ph}^{S=1,T=0}$ is also shown to illustrate the similar behaviour to $\tilde{U}_{pp}^{S=0,T=1}$. The white spaces imply that $\tilde{U}_q^{S,T}$ was not calculated for those parameters. Reasoning is that the Hund's coupling parameter J cannot be larger than the Coulomb interaction parameter U meaning that those parameter regimes are not physical.

excitations. For the particle-hole excitations, a similar pattern to the two particle excitations emerges, with the main difference being that the spin-triplet orbital-singlet is always positive and has a maximum while the spin-singlet orbital-triplet excitation has a negative minimum. Thus, if we switch the spin and orbital states of two particle excitations and switch to the particle-hole excitations, we find that the particle-hole excitations mimic the patterns of the two particle excitations. It should also be noted that in all four of these excitations that the values of $\tilde{U}_q^{S,T}$ are identical for $J = 0$.

3.2 Splitting of the Effective Interaction

The four-vertex can be written in the form [5]

$$\begin{aligned} \Gamma_{m_1\sigma_1 m_2\sigma_2; m_3\sigma_3 m_4\sigma_4} = & \Gamma_C (\delta_{m_1 m_4} \delta_{m_2 m_3} \delta_{\sigma_1 \sigma_4} \delta_{\sigma_2 \sigma_3} - \delta_{m_1 m_3} \delta_{m_2 m_4} \delta_{\sigma_1 \sigma_3} \delta_{\sigma_2 \sigma_4}) \\ & + \Gamma_e (\delta_{m_1 m_3} \delta_{m_2 m_4} \delta_{\sigma_1 \sigma_4} \delta_{\sigma_2 \sigma_3} - \delta_{m_1 m_4} \delta_{m_2 m_3} \delta_{\sigma_1 \sigma_3} \delta_{\sigma_2 \sigma_4}), \end{aligned} \quad (22)$$

where the indices m_i and σ_i are the orbitals and spins of the creation and annihilation operators from which the four-vertex can be calculated. Γ_e vanishes for $J = 0$ [5], thus it should correspond to a kind of effective Hund's coupling interaction. Since this separation into parts is possible for the four-vertex we expect it to also be possible for the effective quasiparticle interaction \tilde{U} .

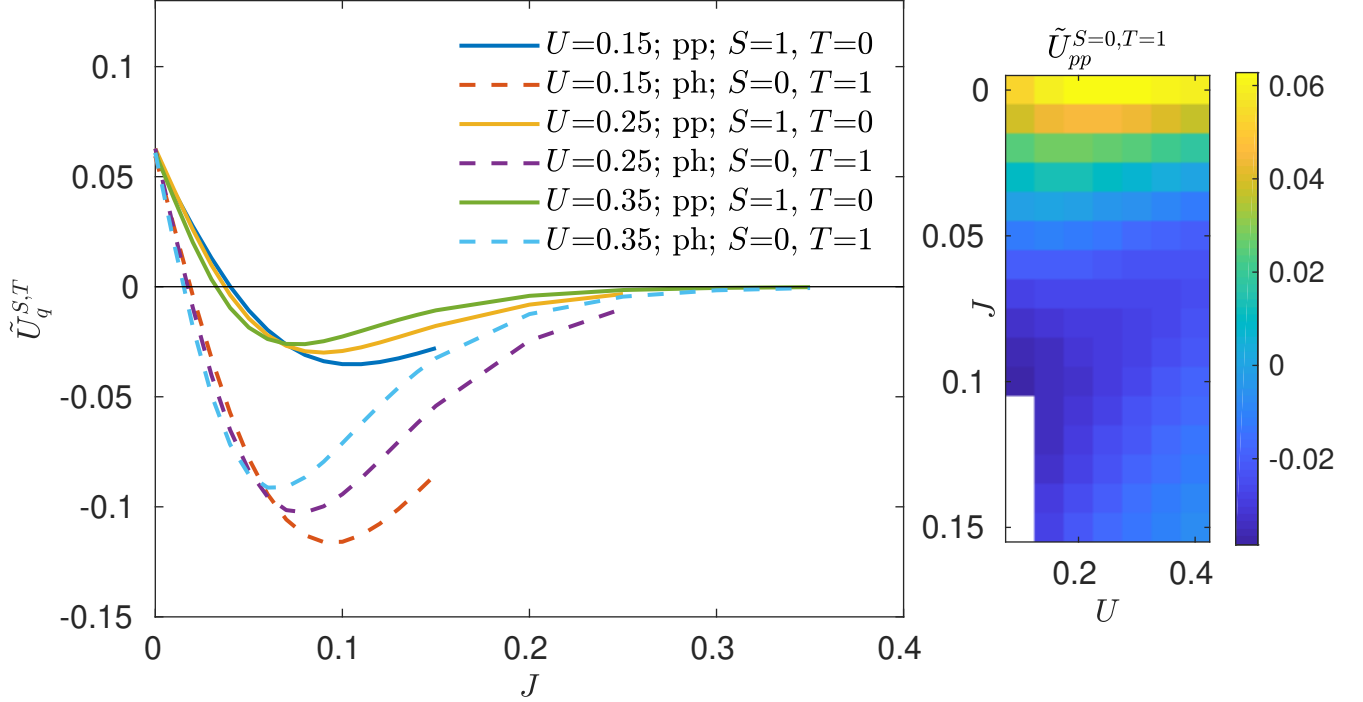


Figure 10: Similar patterns to figure 9, but $\tilde{U}_{pp}^{S=1, T=0}$ is calculated instead, causing there now be a minimum, that is actually negative, instead of a maximum. The line plot also shows $\tilde{U}_{ph}^{S=0, T=1}$ to again show the similarity between the effective two-particle and particle-hole interactions. The white spaces were not calculated as they are not physical.

This separation into two parts is indeed possible giving us two parts, which we call the Coulomb part \tilde{u} and the Hund's coupling part \tilde{j} . The different \tilde{U} can then be written the following way:

$$\begin{aligned}
\tilde{U}_{pp}^{S=0, T=1} &= \tilde{u} + \tilde{j}. \\
\tilde{U}_{pp}^{S=1, T=0} &= \tilde{u} - \tilde{j}. \\
-\tilde{U}_{ph}^{S=0, T=1} &= -\tilde{u} + 2\tilde{j}. \\
-\tilde{U}_{ph}^{S=1, T=0} &= -\tilde{u} - 2\tilde{j}.
\end{aligned} \tag{23}$$

These relations were found by simply looking at the values and behaviour of the different $\tilde{U}_q^{S,T}$.

We can prove that this is indeed the case by solving the equations in (23) for \tilde{u} and \tilde{j} , giving us several ways to calculate them. We will denote them as \tilde{u}_q and \tilde{j}_q with $q \in \{pp, ph, hh\}$ to indicate from what kinds of excitation they were calculated, though since right now we still have a particle-hole symmetry hh parameters will be omitted:

$$\begin{aligned}
\tilde{u}_{pp} &= (\tilde{U}_{pp}^{S=0, T=1} + \tilde{U}_{pp}^{S=1, T=0})/2. \\
\tilde{u}_{ph} &= (\tilde{U}_{ph}^{S=1, T=0} + \tilde{U}_{ph}^{S=0, T=1})/2. \\
\tilde{j}_{pp} &= (\tilde{U}_{pp}^{S=0, T=1} - \tilde{U}_{pp}^{S=1, T=0})/2. \\
\tilde{j}_{ph} &= (\tilde{U}_{ph}^{S=1, T=0} - \tilde{U}_{ph}^{S=0, T=1})/4.
\end{aligned} \tag{24}$$

The different \tilde{u}_q and \tilde{j}_q should of course have the same values since we are trying to reduce the total number of parameters necessary to describe the quasiparticle interaction.

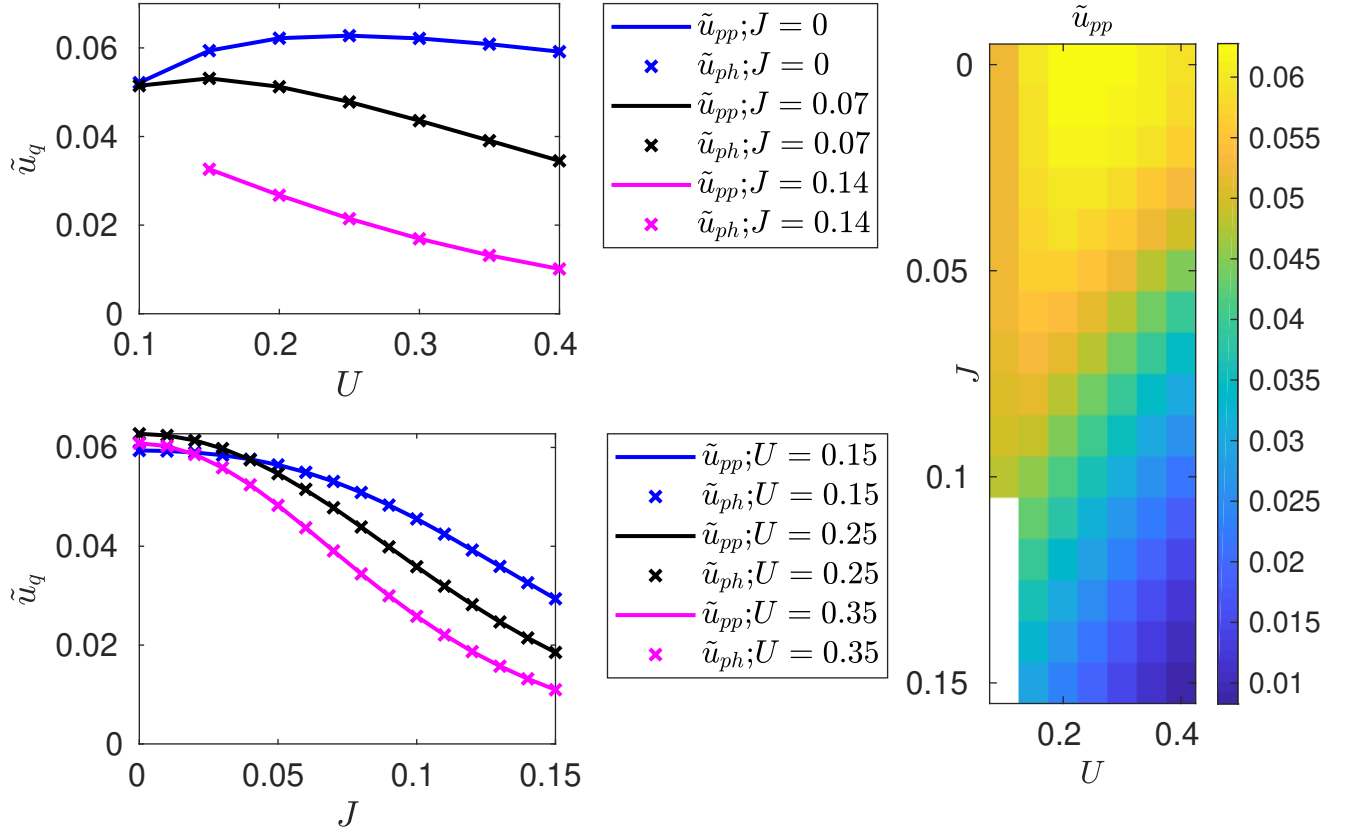


Figure 11: The Coulomb part \tilde{u} of the effective interaction calculated for different U and J , while ϵ_d is chosen such that we find ourselves at half-filling. In the upper left line plot U is varied for different J to illustrate the relatively clear maxima. Meanwhile, the lower left line plot shows \tilde{u} when J is varied with fixed U , resulting in mainly monotonous behaviour. In the line plots the two different \tilde{u}_q denoted by the lower index q are shown. As we can see their values match up exactly.

We plot these parameters against U for fixed J in the upper left corner and against J for fixed U in the lower left corner of figure 11 and 12. The different \tilde{u}_q and \tilde{j}_q can be seen to indeed match up exactly, showing that a simplification of the effective interaction is possible. Therefore, we from now on mainly refer to both \tilde{u}_{pp} and \tilde{u}_{ph} simply as \tilde{u} , unless a distinction is necessary to show how it was calculated. Similarly, the parameters \tilde{j}_{pp} and \tilde{j}_{ph} are referred to as \tilde{j} .

We can see in the lower left line plot of figure 11 that when J is increased it causes a screening effect for \tilde{u} and that the dropoff of \tilde{u} due to the screening becomes faster as U is increased. In contrast, when J is fixed and one varies U , like in the upper left line plot, one can see that there exists a clear maximum. Its value becomes smaller and shifts to smaller U when a larger J is chosen, since the screening strength is increased. To sum up we can say that increasing either J or U causes screening effects which weaken the effective Coulomb interaction \tilde{u} . However U also has a strengthening effect on \tilde{u} , even if at some point the suppression of the fluctuations causes \tilde{u} to converge towards 0 as we have seen before in the single channel case.

For the plots of \tilde{j} in figure 12 a very similar pattern emerges except that the roles of U and J are reversed compared to before. That is to say, a stronger U only causes a screening

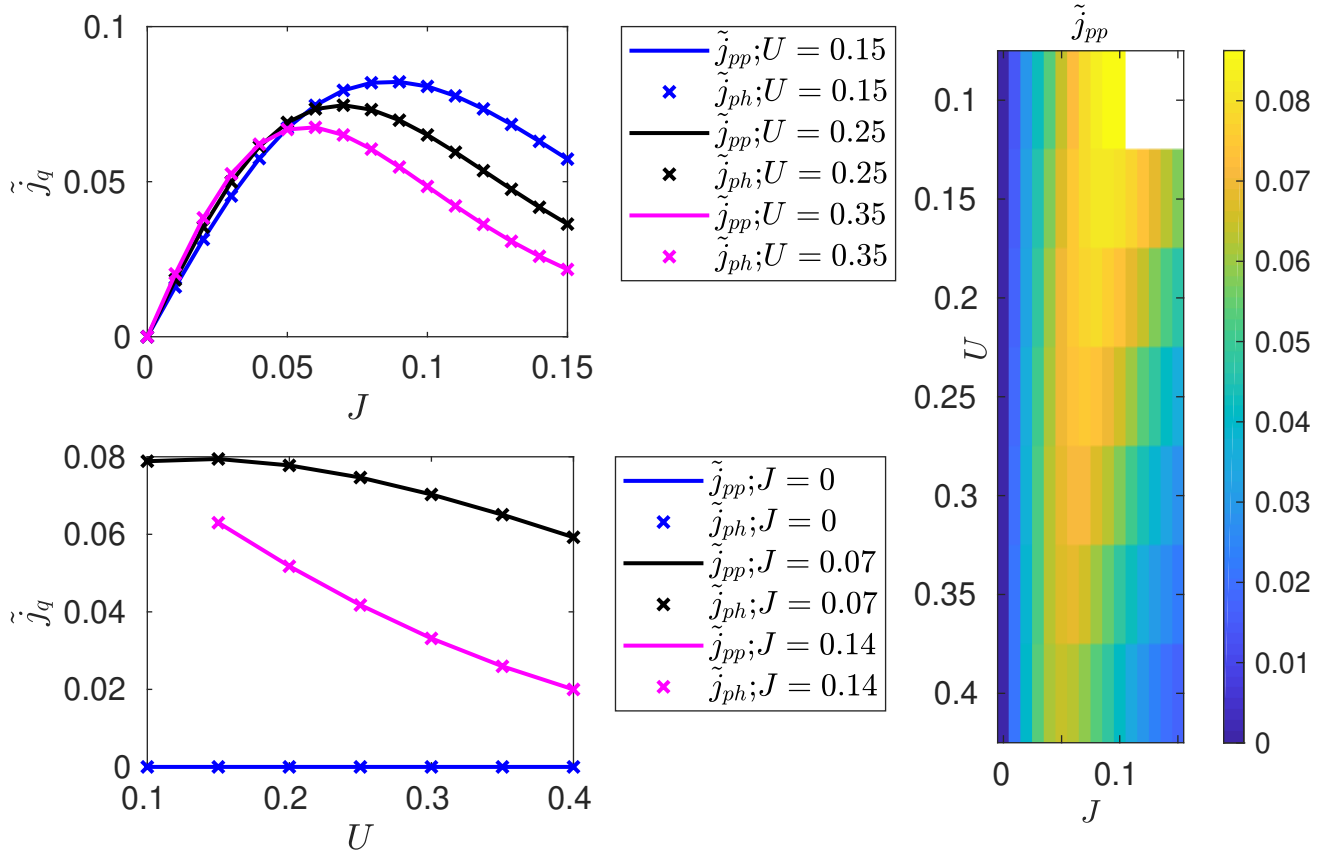


Figure 12: Similar to figure 11, but now it is the Hund’s coupling part \tilde{j} of the effective interaction that is plotted. In the colourplot the positions of the U and J axis have been switched in order to highlight the similarity of \tilde{u} and \tilde{j} if the roles of the bare variables are switched. Similarly, the line plot where J is varied while fixing U is now in the upper left corner to illustrate the clear maximum, and the line plot where U is varied is found in the lower left corner to show the almost monotonous behaviour of \tilde{j} upon varying U . The different ways of calculating \tilde{j}_q can again be seen to result in the same values.

effect for \tilde{j} whereas an increasing J causes screening while also having a strengthening effect on the effective Hund’s coupling, with the former dominating for large J . The result is a clear maximum when fixing U and varying J , of which the value and position changes for different U , which can be seen in the upper left line plot. Additionally, we can see in the lower left line plot that an increase in U again only has a screening-strengthening effect.

It should also be noted that values of \tilde{j} are 0 when $J = 0$, which is expected if \tilde{j} is a kind of effective Hund’s coupling. A similar attribute can be expected for \tilde{u} but that was not calculated, as we would then have a non-interacting system.

The naming scheme of the two parts might be a bit misleading, since both \tilde{u} and \tilde{j} depend on U and J , but it was chosen for intuitive purposes. The same can be said about why the effective particle-hole interactions were written with a minus in (23).

By writing the $\tilde{U}_q^{S,T}$ this way and reminding ourselves that the definition of the $\tilde{U}_{ph}^{S,T}$ are inverted sign-wise, we can see that the sign of the Coulomb part \tilde{u} only depends on the “charges” of our quasiparticles, as two particles should repel each other and a particle and a hole should be attractive. In contrast the sign of the Hund’s coupling part \tilde{j} only depends on S and T , since if $S = 0$ and $T = 1$ \tilde{j} contribute positively, and switching the spin and orbital number

changes the sign before the \tilde{j} .

The decomposition into two parts lets us easily explain the patterns seen in the line plots of figures 9 and 10: When looking at, for example $U_{pp}^{S=0,T=1}$, the Coulomb part and Hund's coupling part are first "working together", but the switch to $S = 1, T = 0$ causes the Hund's coupling part to switch signs. Therefore, the two parts are now "working against each other". For particle-hole excitations the pattern is similar except the Coulomb part is now attractive due to the different "charges". Thus, in the $S = 0, T = 1$ case the two parts are "working against each other" and "working together" in the $S = 1, T = 0$ case.

The decomposition of \tilde{U}_{pp} in the two-particle case actually has the same form as the eigenvalues of the interaction part of the Hamiltonian H_{int} , with the eigenstates being the isolated impurity with two electrons in the spin singlet orbital triplet or spin triplet orbital singlet state denoted by $|S, T\rangle$. The eigenvalue equations are given by

$$\begin{aligned} H_{\text{int}}|S = 0, T = 1\rangle &= (U + J)|S = 0, T = 1\rangle, \\ H_{\text{int}}|S = 1, T = 0\rangle &= (U - J)|S = 1, T = 0\rangle. \end{aligned} \quad (25)$$

The effective interaction energies $\tilde{U}_{ph}^{S=0,T=1}$ and $\tilde{U}_{ph}^{S=1,T=0}$ can at least still be explained this way, by assuming the Hund's coupling part to be twice as strong and making arguments based on the "charges". However, the interactions corresponding to other excitations cannot be explained the same way as we will see .

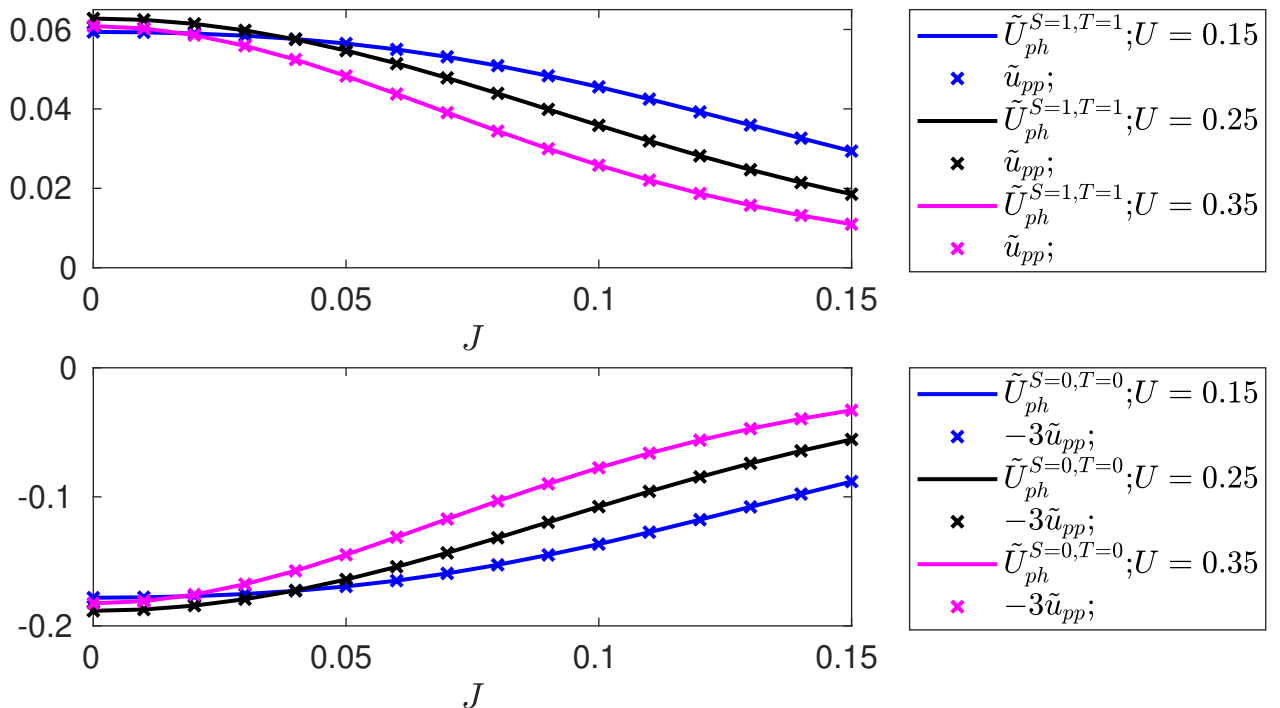


Figure 13: In both line plots we vary J while fixing U . The upper plot shows the values of $\tilde{U}_{ph}^{S=1,T=1}$ and \tilde{u}_{pp} . The lower plot is similar but now $\tilde{U}_{ph}^{S=0,T=0}$ and $-3\tilde{u}_{pp}$ are plotted instead. According to (26) the values in both plots are identical, which is indeed what we see.

In this thesis we do not discuss two-particle excitations where both the spin and the orbital number are triplet states or singlet states, as these are relatively high energy excitations. As

we already mentioned, the NRG procedure becomes less accurate for higher energies such that the calculation of the renormalized parameters from the higher parts of the spectrum becomes impossible.

Double-singlet and double-triplet particle-hole excitations however are still low enough in the energy spectrum to be accurately calculated via NRG, such that we can use them to calculate the effective interaction energies. These \tilde{U} can be described with the Coulomb part from before:

$$\begin{aligned} -\tilde{U}_{ph}^{S=0,T=0} &= 3\tilde{u}. \\ -\tilde{U}_{ph}^{S=1,T=1} &= -\tilde{u}. \end{aligned} \tag{26}$$

The veracity of these equations is proven in figure 13, where we plot in the upper plot $U_{ph}^{S=1,T=1}$ and \tilde{u} against J for different U . In the lower plot the same is done for $U_{ph}^{S=0,T=0}$ and $-3\tilde{u}$. We can again see that the values line up very well.

It should be noted that the results for $\tilde{U}_{ph}^{S=0,T=0}$ might not be completely correct, since one needs to select the excitation corresponding to $[000]$, which is the ground state. Therefore, one needs to select the next highest line, but it might not actually correspond to the lowest energy excitation. A possible interpretation of $U_{ph}^{S=1,T=1}$ could be the effect of the two triplet states cancelling each other out. This explanation however would also not match up with the similarity stated in (25) as the double triplet state has the eigenvalue $U + J$, which should correspond to $U - J$ after adjusting the signs according to the logic used before.

3.3 Calculations of the Parameters for Large U and J at Half-Filling

We now take a look at the behaviour in the case of large U and J , while still staying at half-filling.

For rather large U and J the charge, spin and orbital fluctuations are suppressed, therefore the corresponding susceptibilities can be set to 0. This gives us a relation between \tilde{u} and \tilde{j} as was shown by Nishikawa et al. [4], though in our case the definitions of the Hamiltonian and the decomposition into parts differ resulting in the relation

$$2\tilde{u} = \tilde{j}. \tag{27}$$

This becomes evident in figure 14 where we plotted $2\tilde{u}$ and \tilde{j} against J for different U . As we can see, the two lines start to converge for higher J and the convergence is faster if U is larger. Hewson et al. has shown that for large U in the single-channel case \tilde{U} and $\frac{\pi}{2}\tilde{V}^2$ converge to a single energy scale, the Kondo temperature [3]. Therefore, we expect that in the two-orbital case \tilde{u} , \tilde{j} and $\frac{\pi}{2}\tilde{V}^2$ also converge to a single energy scale for large U . Indeed, this is shown in figure 15 where we plotted \tilde{u} , $\tilde{j}/2$ and $\frac{\pi}{2}\tilde{V}^2$ against U . If this single energy scale corresponds to the Kondo temperature is not known, but in analogy to the single-channel it is expected. In the upper plot this is done only at $J = 0.05$ to better illustrate the difference between the three parameters. In the lower plot three different J are chosen to show that in order for the convergence to take place, a specific J is not necessary. In fact, we can see that the parameters converge faster for larger J , probably due to the additional suppression of orbital fluctuations.

In figure 16 we plot Z against U and J , which shows us that Z behaves monotonously upon variation of U and J . The quasiparticle weight has its largest value for small J and U being almost 1 for $J = 0$ and $U = 0.1$. It also converges to 0 when either J or U is increased. This

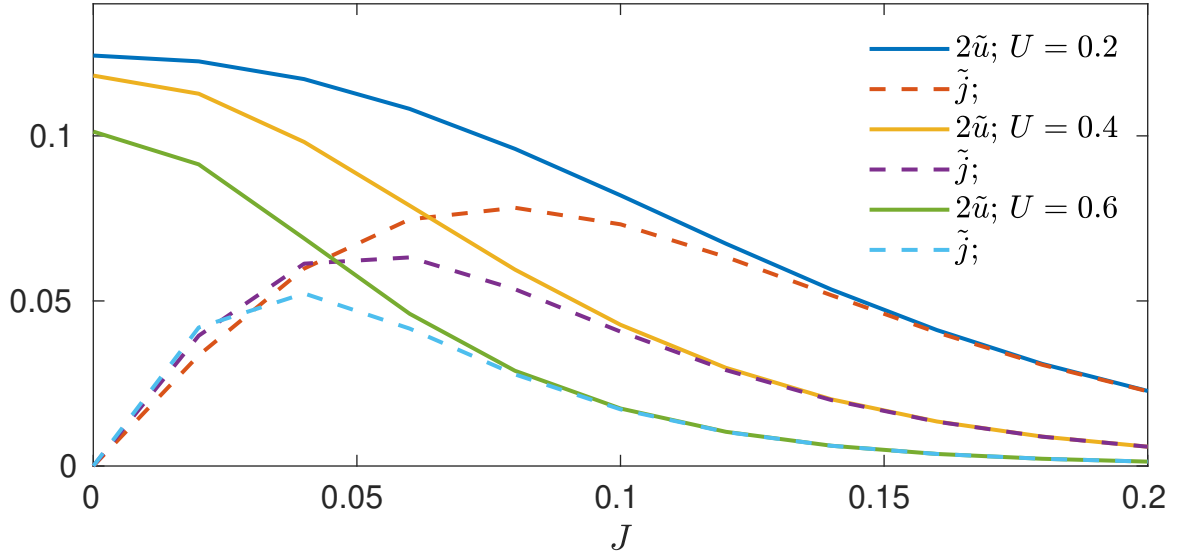


Figure 14: Plotting $2\tilde{u}$ and \tilde{j} against J for different U to illustrate their equivalence when fluctuations are suppressed. When U is larger the convergence is significantly faster.

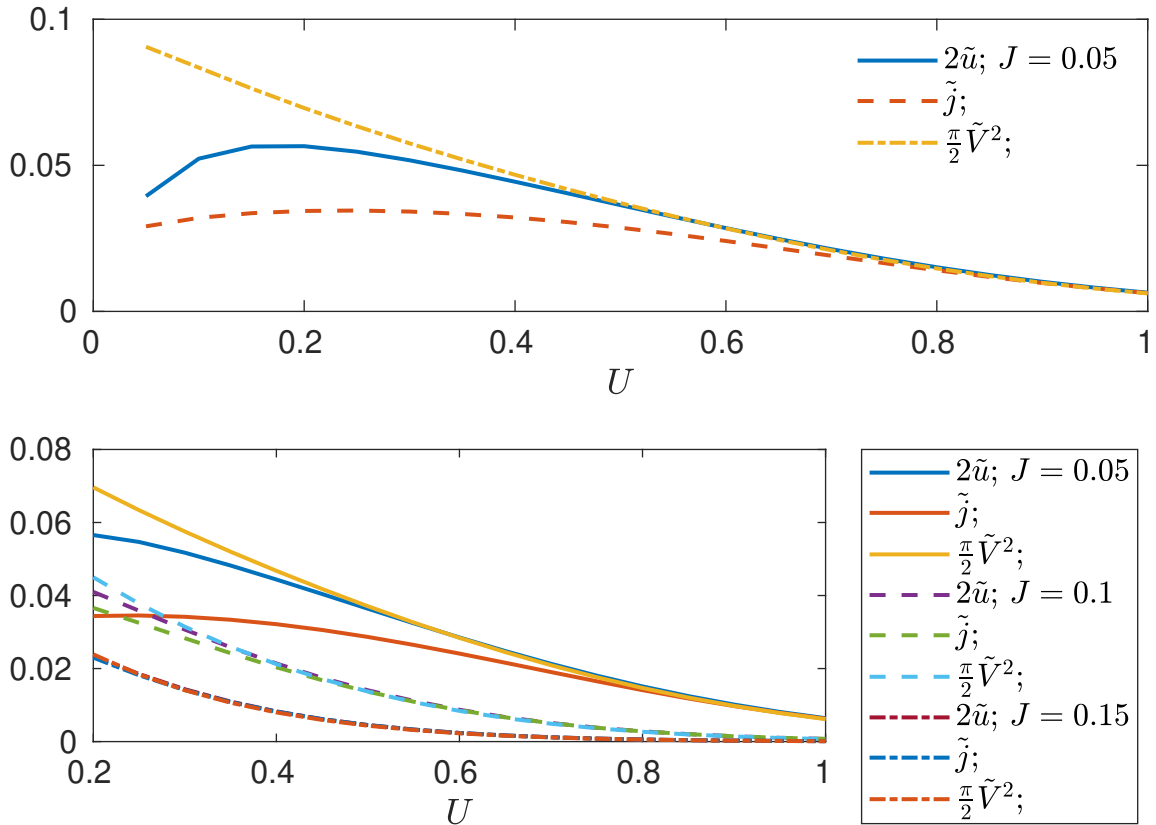


Figure 15: In both plots $2\tilde{u}$, \tilde{j} and $\frac{\pi}{2}\tilde{V}^2$ are plotted against U for fixed J . In the upper plot we can see how all three parameters converge to a single energy scale. In the lower plot the three parameters are harder to differentiate, but the different values of J shows that this convergence does not require a specific J to take place.

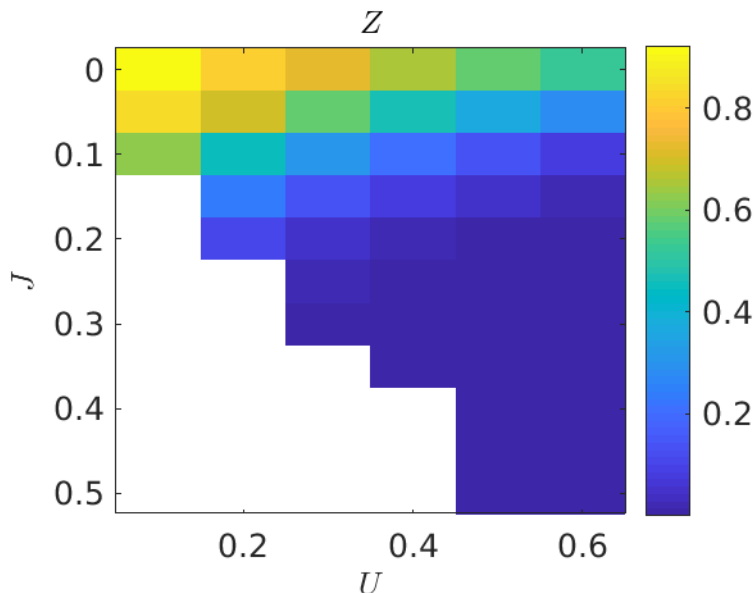


Figure 16: Z plotted against U and J at half-filling in a colour plot. We can see that Z decreases monotonously when either U or J are increased, while converging to 1 when both interaction parameters approach 0.

was expected for the same reason as before; if the interaction parameters U and J go towards 0 then the Fermi liquid transitions to a non-interacting system implying a quasi-particle weight of 1. Larger U and J also imply stronger physical interactions which again implies that the correlation strength increases between the electrons, resulting in a small Z .

According to (16) Γ is given by the fraction U/Z^2 . Since we showed before that for large U and J the parts of the effective interaction \tilde{U} and $\tilde{V}^2 = Z \cdot V^2$ take on the same energy scale we can conclude that $\Gamma \propto 1/Z$ in this parameter regime. Thus, Γ diverges when Z converges to 0, which is again expected as Γ is the sum of all orders of the interactions, which are expected to become larger if the interaction strength parameters U and J are increased.

3.4 Effective Interaction with Broken Particle-Hole Symmetry

Until now, two-particle excitation energies have been completely identical to two-hole excitation energies as we have been at half-filling. If we move away from that, particle-hole symmetry is broken, which could lead to differing \tilde{U}_{pp} and \tilde{U}_{hh} . However, since we expect the Coulomb action part of the interaction to be the same, due to the same charges, and the Hund's coupling's contribution to also be the same, as long as we choose identical spin and orbital number states for the excitations, we expect that \tilde{U}_{pp} and \tilde{U}_{hh} converge towards the same value for large N . This is indeed what we find as long as the NRG calculations are accurate.

This can be seen in figure 17, where we plot $\tilde{U}^{S=1, T=0}$, one time calculated from two particle excitations and the other time from two hole excitations, against ϵ_d/U starting from half-filling for different J and $U = 0.2$. It is clear that the two ways of calculating result in values that match very well. It should be noted that more realistic values of J were chosen, as in $U/2 \geq J$. This was done as high values of J result in peculiar behaviour around half filling.

For the more realistic J values however a similar pattern to the single channel case emerges; the minimum of the interaction is again found at half filling. Thus for most values of J a negative $\tilde{U}^{S=1, T=0}$ is only found around half filling, since only then does the value of the minimum drop below 0.

In the empty orbital regime it appears that \tilde{U} is proportional to J . Therefore it is also possible

to have a negative \tilde{U} even in the full orbital/empty orbital regime, as long as the chosen J are very large.

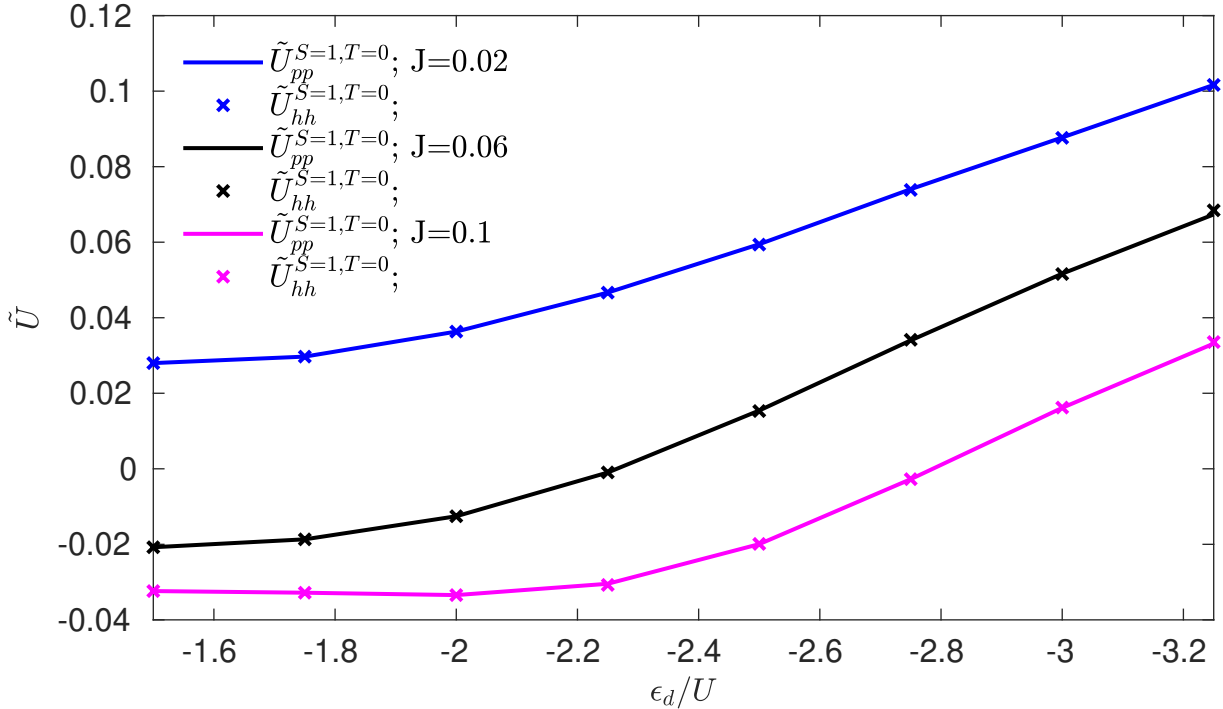


Figure 17: The effective interaction $\tilde{U}^{S=1,T=0}$ plotted against ϵ_d/U for different J and $U = 0.2$. The initial ϵ_d/U corresponds to half-filling. The lines were calculated via two particle excitations and the crosses via two hole excitations. As we can see, their values match up exactly.

In the last section we also split the effective interaction into two parts, which can be used to describe both two-particle and particle-hole effective interactions. Since the different $\tilde{U}_{hh}^{S,T}$ are equivalent to their $\tilde{U}_{pp}^{S,T}$ counterparts, they can be decomposed the same way. Similar to the single-channel case, we only expect this equivalence when the number of sites is large enough to consider our system a Fermi liquid. This is shown in figure 18 where we plotted the different \tilde{u}_q and \tilde{j}_q against the number of sites N with $\epsilon_d = -2U = -4J = -0.4$. These parameters are chosen such that we do not have identical particle and hole excitation energies. We can see that only for sufficiently large U and J do the different \tilde{u}_q converge towards a single value and the same pattern can be seen for the 3 different \tilde{j}_q . The dropoff at the end is due to numerical instabilities, which were mentioned before in Section 2.2.

4 Conclusion

We have outlined how to calculate the renormalized parameters $\tilde{\epsilon}_d$, $\tilde{\Delta}$ and \tilde{U} through the bare parameters of the Anderson impurity model. This includes how the the excitation energies necessary for the calculation are selected from the flow diagrams, that are calculated via NRG. The calculation methods of the quasiparticle weight Z and four-vertex Γ were also covered. We have also shown that calculating these parameters by combining NRG and RPT requires significantly less computational power than doing so via dynamic results of NRG, while providing more accurate results.

We then calculated the values of our parameters of interest in the single-channel case while varying the impurity level energy ϵ_d and the Coulomb interaction strength U , which is the only

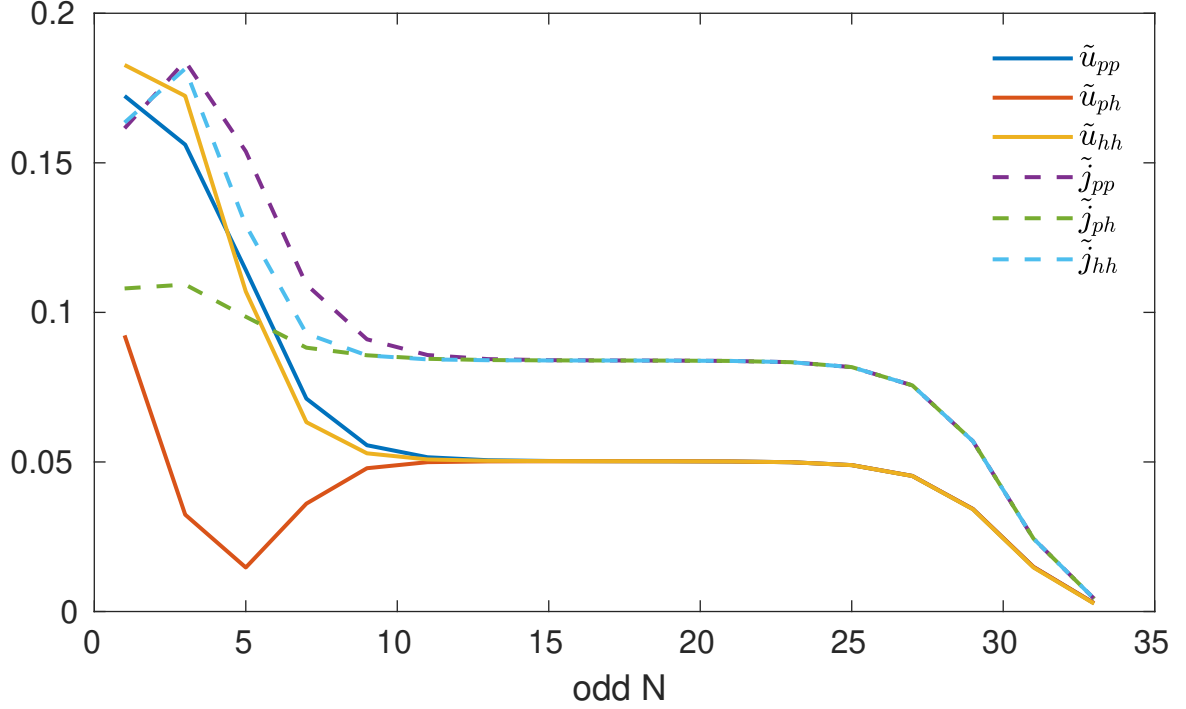


Figure 18: The different \tilde{u}_q and \tilde{j}_q plotted against the number of bath sites N for $\epsilon_d = -2U = -4J = -0.4$. The different \tilde{u}_q and \tilde{j}_q converge to their respective values for large enough N .

kind of interaction in our single channel model. From those results we can conclude that the correlation strength increases the closer one is to half-filling and the larger U is. Additionally, an increase correlation strength also increases the screening strength.

In the two-channel case we still had a single energy level ϵ_d for both orbitals, but Hund's coupling was added to the interaction term, with the strength of the coupling being determined by the bare parameter J . We then calculated the effective interaction similar to the single-channel case. However, this time we varied the interaction strengths U and J at half-filling, while differentiating between the different possible spin and orbital states that the double excitations can be found in. We discovered that all the effective interactions for all the different excitations can be written as a linear combination of an effective Coulomb part \tilde{u} and an effective Hund's coupling part \tilde{j} . The effective Hund's coupling part actually tends to be larger than \tilde{u} , causing the effective interaction between two electrons to actually be attractive if the appropriate spin and orbital numbers S and T are chosen. For the effective interaction between particles and holes $\tilde{U}_{ph}^{S,T}$ the influence of the \tilde{j} is twice as strong in comparison to the effective interaction between two particles $\tilde{U}_{pp}^{S,T}$. We also observed that as U and J are increased $\tilde{j}/2$, \tilde{u} and the effective hybridization \tilde{V}^2 converge to a single energy scale and that the correlation strength increases causing \tilde{u} and \tilde{j} to experience stronger screening. At the end we briefly looked at the case that particle-hole symmetry is broken, where we showed that the minimum is still found at half-filling and that the effective interaction between holes $\tilde{U}_{hh}^{S,T}$ is identical to the effective interaction between particles $\tilde{U}_{pp}^{S,T}$.

In this thesis a lot of aspects were only briefly mentioned but never looked into. Further research should consider looking into some of the following possibilities: Checking if the single energy scale for large U and J in two-orbital case actually corresponds to the Kondo temperature and having different orbital level energies, i.e. $\epsilon_{d,m}$ depending on the index m . Some of the observations made could also not be properly explained, e.g. the doubling of

the effective Hund's coupling for particle-hole excitations. Explaining these features might require a stronger theoretical background or more accurate calculations in order to analyze the higher-energy excitations.

References

- [1] Ralf Bulla, Theo A. Costi, and Thomas Pruschke. Numerical renormalization group method for quantum impurity systems. *Reviews of Modern Physics*, 80(2):395–450, 2008.
- [2] Antoine Georges, Gabriel Kotliar, Werner Krauth, and Marcelo J. Rozenberg. Dynamical mean-field theory of strongly correlated fermion systems and the limit of infinite dimensions. *Reviews of Modern Physics*, 68(1):13–125, 1996.
- [3] A. C. Hewson, A. Oguri, and D. Meyer. Renormalized parameters for impurity models. *The European Physical Journal B*, 40(2):177–189, 2004.
- [4] Y. Nishikawa, D. J. G. Crow, and A. C. Hewson. Renormalized parameters and perturbation theory for an n -channel anderson model with hund's rule coupling: Symmetric case. *Physical Review B*, 82(11), 2010.
- [5] A. Yoshimori. Perturbation analysis on orbital-degenerate anderson model. *Progress of Theoretical Physics*, 55(1):67–80, 1976.

Acknowledgements

I first and foremost want to thank my family, as they have been supporting me throughout all of my entire studies in physics. Especially my parents since without their financial support I would not be able to dedicate myself to my education to the extend I do.

The person who has directly helped me the most during the writing of this Bachelor thesis is Fabian Kugler. He always pointed me in the direction in which I should look into the behaviour of the model and explained many concepts to me. The code that sets up the Hamiltonian and applies the NRG procedure to it was also written by him.

I also want do thank Seung-Sup Lee and Andreas Weichselbaum for providing the NRG code. Lastly, I want to thank Professor Delft for letting me write at his chair and providing the means to do the necessary calculations.

Hiermit erkläre ich, die vorliegende Arbeit selbständig verfasst zu haben und keine anderen als die in der Arbeit angegebenen Quellen und Hilfsmittel benutzt zu haben.

München, Datum der Abgabe
Unterschrift